

Spectral Quantum Beating in Mixed Frequency/Time-Domain Coherent Multidimensional Spectroscopy

Andrei V. Pakoulev, Mark A. Rickard, Nathan A. Mathew, Kathryn M. Kornau, and John C. Wright*

Department of Chemistry, University of Wisconsin, Madison, Wisconsin 53706

Received: March 9, 2007; In Final Form: May 17, 2007

Coherent multidimensional spectroscopy performed in the mixed frequency/time domain exhibits both temporal and spectral quantum beating when two quantum states are simultaneously excited. The excitation of both quantum states can occur because either the spectral width of the states or the excitation pulse exceeds the frequency separation of the quantum states. The quantum beating appears as a line that broadens and splits into two peaks and then recombines as the time delay between excitation pulses increases. The splitting depends on the spectral width of the excitation pulses. We observe the spectral quantum beating between the two nearly degenerate asymmetric carbonyl stretch modes in a nickel tricarbonyl chelate using the nonrephasing, ground state bleaching coherence pathway in triply vibrationally enhanced four-wave mixing as the time delay between the first two excitation pulses changes.

Introduction

In time-domain ultrafast spectroscopy, the bandwidth of typical excitation pulses is sufficient to simultaneously excite multiple coherences with different frequencies. The time-domain output then exhibits quantum beating from the interference of coherences with different frequencies, and Fourier transformation displays a frequency-domain spectrum of the quantum states.^{1–4} Time-domain coherent multidimensional spectroscopy (CMDs) uses a series of excitation pulses that excite a series of quantum mechanical coherences, populations, or both.^{5–8} The coherences form a temporally and spatially coherent array of oscillators that emit a directional beam defined by phase matching. Changing the time delays between the input pulses creates temporal beating between coherences, and Fourier transforming the coherences' temporal dependence creates multidimensional spectra over a range defined by the excitation pulse bandwidth. Cross-peaks appear in the spectra when quantum states are coupled by intra- or intermolecular interactions. Phase coherence is required between the excitation pulses over the entire measurement time.

Frequency-domain CMDs methods such as doubly vibrationally enhanced (DOVE) and triply vibrationally enhanced (TRIVE) four-wave mixing (FWM) measure the signal enhancements as a function of the excitation frequencies.^{9–13} The excitation pulses are long, and their bandwidth is narrower than the transitions, so any pulse typically excites only single transitions. The accessible frequency range is defined only by the tuning range of the excitation sources, and phase coherence is required only during the time the excitation pulses are present. Temporal information is contained in the transition line shapes. Mixed frequency/time-domain DOVE- and TRIVE-FWM measurements use pulses with intermediate spectral widths that are comparable to the widths of the transitions and temporal widths that are comparable to the transition lifetime.^{14–19} The multidimensional spectra are measured in the frequency domain from the signal enhancement dependence on the excitation frequencies. The dynamics are measured in the time domain from the

signal enhancement dependence on the excitation pulse time delays. This approach allows one to define a specific coherence pathway and the specific quantum states involved in the pathway. In particular, it allows one to isolate the coherence transfer pathways that show the interstate couplings.¹⁴

In this paper, we report the frequency-domain manifestation of quantum beating. The frequency-domain quantum beating appears as a spectral line-splitting that oscillates as a function of the time delay between the first and second excitation pulses and has a period defined by the frequency difference between the coherences. It resolves two closely spaced states that are unresolved in conventional infrared spectra. The quantum beating occurs only when two or more quantum states overlap with the narrow excitation bandwidth, either because the width of the states prevents their resolution or because the frequency difference between the states is less than the excitation bandwidth. We show how the temporal and spectral characteristics of quantum beating change as the excitation pulse widths change from the impulsive to the continuous wave limit. We also show that the magnitude and the phase of the periodic oscillation of the splitting are defined by the excitation pulses' spectral width and the quantum states' dephasing rates.

Experimental

The TRIVE-FWM experiments were performed using two optical parametric amplifiers (OPAs) that were pumped by a Ti:sapphire regenerative amplifier. The difference frequency between the signal and idler of each OPA provided two tunable infrared excitation beams, ω_1 and ω_2 . The ω_2 beam was split to create a k_2 and a k_2' beam. The excitation beams were focused into a sample at angles in a box phase matching geometry such that $k_4 = k_1 - k_2 + k_2'$, where each k -vector is labeled according to its frequency. The excitation pulses were 900 fs wide and have an 18 cm⁻¹ fwhm. Delay lines adjusted the relative time delays, $\tau_{21} \equiv \tau_2 - \tau_1$ and $\tau_{2'1} \equiv \tau_{2'} - \tau_1$, between the k_1, k_2 , and k_2' pulses. A monochromator with a HgCdTe₂ detector measured the FWM output beam at a frequency ω_m . Five variables control the TRIVE-FWM spectroscopy: ω_1 , ω_2 , ω_m , τ_{21} , and $\tau_{2'1}$. Experiments acquire two-dimensional cross sections through this

* To whom correspondence should be addressed. E-mail: wright@chem.wisc.edu.

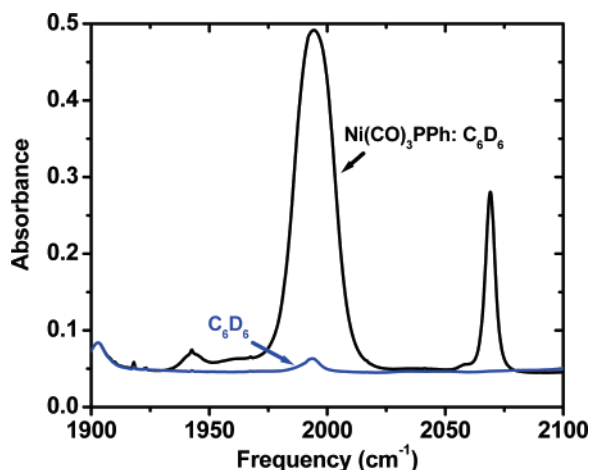


Figure 1. FTIR spectrum of $\text{Ni}(\text{CO})_3(\text{PPh}_3)$ in C_6D_6 (black line) and pure C_6D_6 .

five-dimensional space, typically by measuring the FWM intensity as a function of two variables and fixed values of the other three. For the experiments described in this paper, the time delays were set to values that resulted in the following temporal ordering of the excitation pulses: \bar{k}_2 , \bar{k}_1 , and \bar{k}_3 . The monochromator was tuned so $\omega_m = \omega_1$. These experimental choices define a single coherence pathway that is labeled pathway $\text{VI}\alpha$.^{15,16} It corresponds to the nonrephasing, ground state bleaching pathway in 2D-IR or transient grating experiments. The first excitation creates a coherence between a vibrational state and the ground state. The second excitation pulse creates a ground state population grating. The third excitation creates a second coherence between a vibrational state (which can be different or the same as that in the first coherence) and the ground state. This last coherence forms a spatially and temporally coherent array of oscillators that emits the directional output beam.

The sample was the organometallic complex $\text{Ni}(\text{CO})_3(\text{PPh}_3)$ (abbreviated as NTC). It was synthesized from a 10 mM $\text{Ni}(\text{CO})_2(\text{PPh}_3)_2$ tetrahydrofuran solution that was converted to the NTC by oxidation in the air. After 3 h, the solvent was evaporated under a nitrogen atmosphere, and the remaining solid was dissolved in deuterated benzene. The oxidation formed also NiO solid that was removed by filtration. NTC has tetrahedral geometry and three carbonyl vibrational modes. The asymmetric

stretch modes are labeled a_1 and a_2 , and the symmetric carbonyl stretch is labeled b . The two asymmetric stretches are nearly degenerate and are not resolved in the infrared spectrum.

Figure 1 shows the Fourier transform infrared spectrum (FTIR) of the NTC/ C_6D_6 solution (black line) and pure C_6D_6 (blue line) with a 200 μm path length. The two asymmetric stretches are centered near 1995 cm^{-1} , and the symmetric stretch appears at 2069 cm^{-1} . A reasonable fit of the asymmetric stretch region can be made with a single Gaussian peak centered at 1995 cm^{-1} and a fwhm of 18 cm^{-1} (Figure 2a). The only discrepancy is the small difference at the top of the peak. A better fit requires two Gaussian peaks, one centered at 1990 cm^{-1} with a fwhm of 13 cm^{-1} and one at 1999 cm^{-1} with a fwhm of 12 cm^{-1} (Figure 2b). The FTIR spectrum and fits, although suggestive, do not definitively confirm that the asymmetric stretches in NTC have different frequencies.

Theoretical Model of Quantum Beating. In TRIVE-FWM, transitions occur from the ground state labeled g to two vibrational modes labeled a and b , where a and b can represent any two vibrational states. There are 12 coherence pathways consisting of six time orderings (labeled I–VI) involving either parametric (labeled α) or nonparametric (labeled β) pathways.^{15,16,18,19} For example, the parametric and nonparametric pathways for time ordering VI are $gg \xrightarrow{2'} ag \xrightarrow{-2} gg \xrightarrow{1} bg$ ($\text{VI}\alpha$) and $gg \xrightarrow{2'} ag \xrightarrow{-2} aa \xrightarrow{1} (a+b)a$ ($\text{VI}\beta$), respectively, where the letters represent the diagonal and off-diagonal density matrix elements for the coherences and populations of states g , a , b , and $(a+b)$ and the numbers above the arrows label the frequencies of the three excitation beams. For the case presented in this work, the second interaction can also access a different, nearby vibrational state and create a zero quantum coherence by the pathway $gg \xrightarrow{2'} a_1g \xrightarrow{-2} a_1a_2 \xrightarrow{1} (a_1+b_1)a_2$. This paper uses TRIVE pathway $\text{VI}\alpha$ as a specific example of frequency-domain quantum beating. Other pathways also exhibit quantum beating. The bg density matrix element for pathway $\text{VI}\alpha$ is

$$\rho_{bg}(t, \tau_1, \tau_2, \tau_2') \propto \zeta \int_{-\infty}^{\infty} \int_{-\infty}^{\infty} \int_{-\infty}^{\infty} E(\omega_2, t_a - \tau_2') G_{ag}(t_b - t_a) E(\omega_2, t_b - \tau_2) G_{gg}(t_c - t_b) E(\omega_1, t_c - \tau_1) G_{bg}(t - t_c) dt_a dt_b dt_c \quad (1)$$

where ζ contains the sign and proportionality factors, $E(\omega_i, t - \tau_i) = e^{-i\omega_i(t-\tau_i) - ((t-\tau_i)^2)/(\sigma_i^2)}$ is the excitation electric field, $G_{mn}(t)$

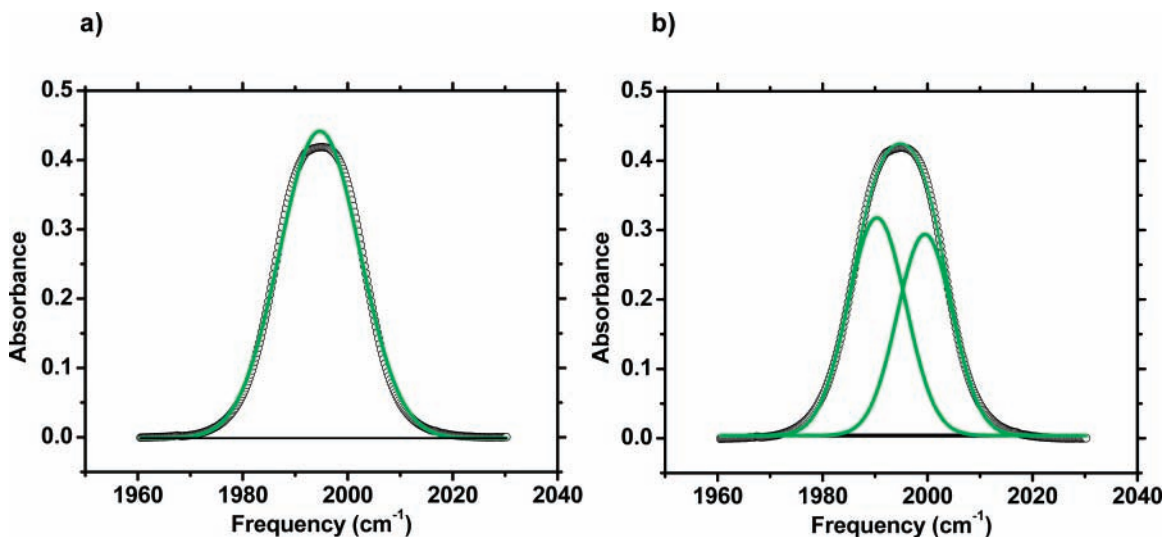


Figure 2. Fit of the $\text{Ni}(\text{CO})_3(\text{PPh}_3)$ peak at 1996 cm^{-1} with (a) a single Gaussian peak and (b) two Gaussian peaks. The black and green curves represent the data and fits, respectively.

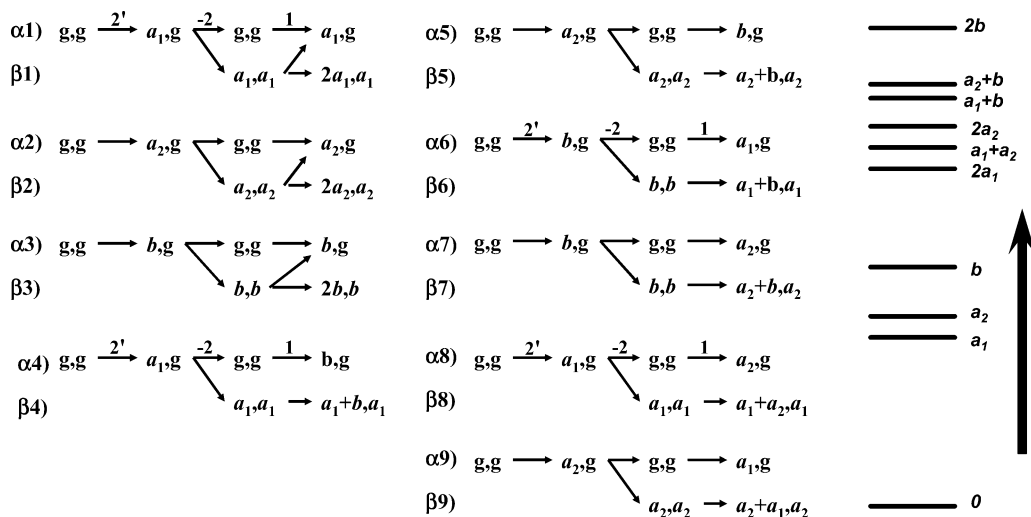


Figure 3. The VI α and VI β coherence pathways with states shown on the right side.

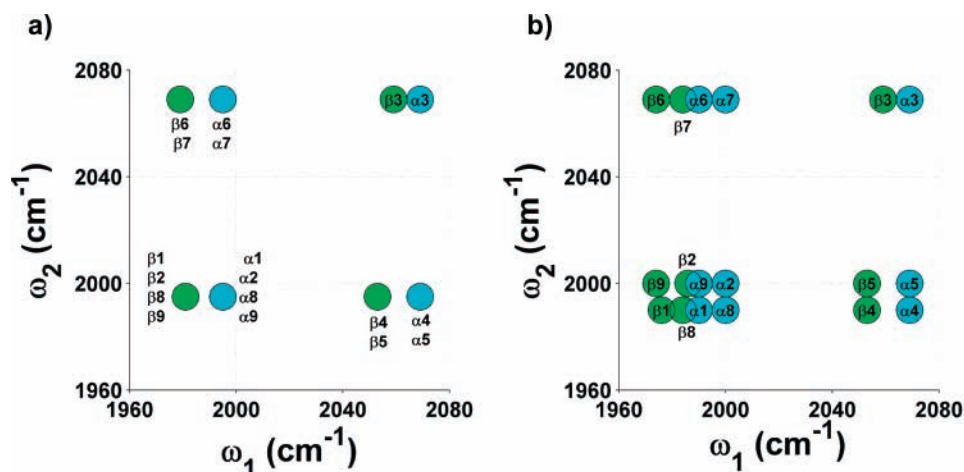


Figure 4. Schematic diagram indicating the positions of the peaks corresponding to each of the pathways sketched in Figure 3. (a) The positions when the two asymmetric modes are degenerate and (b) the positions when they are split. The peak positions correspond to vibrational states with energies $a_1 = 1990 \text{ cm}^{-1}$, $a_2 = 1999 \text{ cm}^{-1}$, and $b = 2069 \text{ cm}^{-1}$.

$= \theta(t) e^{-i\omega_{mn}t - \Gamma_{mn}t}$ is the molecular response involving the mn density matrix element (frequency ω_{mn} and dephasing rate Γ_{mn}), $\theta(t) \equiv 0$ when $t < 0$ and $\theta(t) \equiv 1$ when $t \geq 0$ and the integration is performed over the three interaction times.²⁰ Numbers label the excitation field variables (ω_i , τ_i , σ_i), and letters label the time ordered interaction times: t_a, t_b, t_c where $t_a < t_b < t_c$. This equation has two resonances when $\omega_2 = \omega_{ag}$ and $\omega_1 = \omega_{bg}$. The comparable equation for the VI β pathway has resonances when $\omega_2 = \omega_{ag}$ and $\omega_1 = \omega_{a+b,a}$.

For this paper, the vibrational states can be any of the fundamentals, overtones, and combination bands of the a_1 , a_2 , and b vibrational states shown in Figure 3. For three vibrational states, coherence pathways VI α and VI β create 18 different peaks in two-dimensional spectra of the intensity as a function of ω_1 and ω_2 . Figure 3 describes the state evolution for each spectral feature, and Figure 4 shows a schematic two-dimensional vibrational spectrum of these peaks. If states a_1 and a_2 are degenerate, the 2D ω_1/ω_2 spectrum for NTC will resemble the schematic in Figure 4a. The alpha pathways are parametric pathways that involve only fundamental modes and are colored cyan; the beta pathways are nonparametric pathways that involve overtones or combination bands and are colored green. The 2D schematic spectrum changes if a_1 and a_2 are not degenerate (Figure 4b). The frequency shifts create two coherence pathways that interfere constructively or destructively at the quantum level with other nearby pathways. For these

reasons, a 2D TRIVE spectrum is much more sensitive to the frequencies of the fundamental modes than a linear spectrum.

This paper is concerned with the quantum beating when the two unresolved a_1 and a_2 vibrational states are excited with the first excitation pulse (frequency ω_2) as the excitation pulse width varies from the impulsive to the continuous wave (cw) limit. The two coherences that beat are probed at some later time, τ , by the second and third excitation pulses. In order to obtain a closed form solution, we consider that the first excitation results from a square excitation pulse centered at $\tau_2 = 0$ with a full width of $2s$. For states a_1 and a_2 , the polarization is then

$$\rho(\tau) \propto \int_{-s}^s E^o(\omega_2) e^{-i\omega_2 t_a} (e^{-i(\omega_{a1g} + \Gamma_{a1g})(\tau - t_a)} + e^{-i(\omega_{a2g} + \Gamma_{a2g})(\tau - t_a)}) dt_a \quad (2)$$

Integrating ρ and assuming that $\tau > s$ yields eq 3 with $\Delta_{a,b} = \omega_{a,b} - \omega_2$, where ω_2 is the center frequency of the laser.

$$\rho(\tau) = \frac{e^{(-i\omega_{a1g} - \Gamma_{a1g})\tau}}{i\Delta_{a1g} + \Gamma_{a1g}} (e^{i\Delta_{a1g}s + \Gamma_{a1g}s} - e^{-i\Delta_{a1g}s - \Gamma_{a1g}s}) + \frac{e^{(-i\omega_{a2g} - \Gamma_{a2g})\tau}}{i\Delta_{a2g} + \Gamma_{a2g}} (e^{i\Delta_{a2g}s + \Gamma_{a2g}s} - e^{-i\Delta_{a2g}s - \Gamma_{a2g}s}) \quad \text{for } \tau > s \quad (3)$$

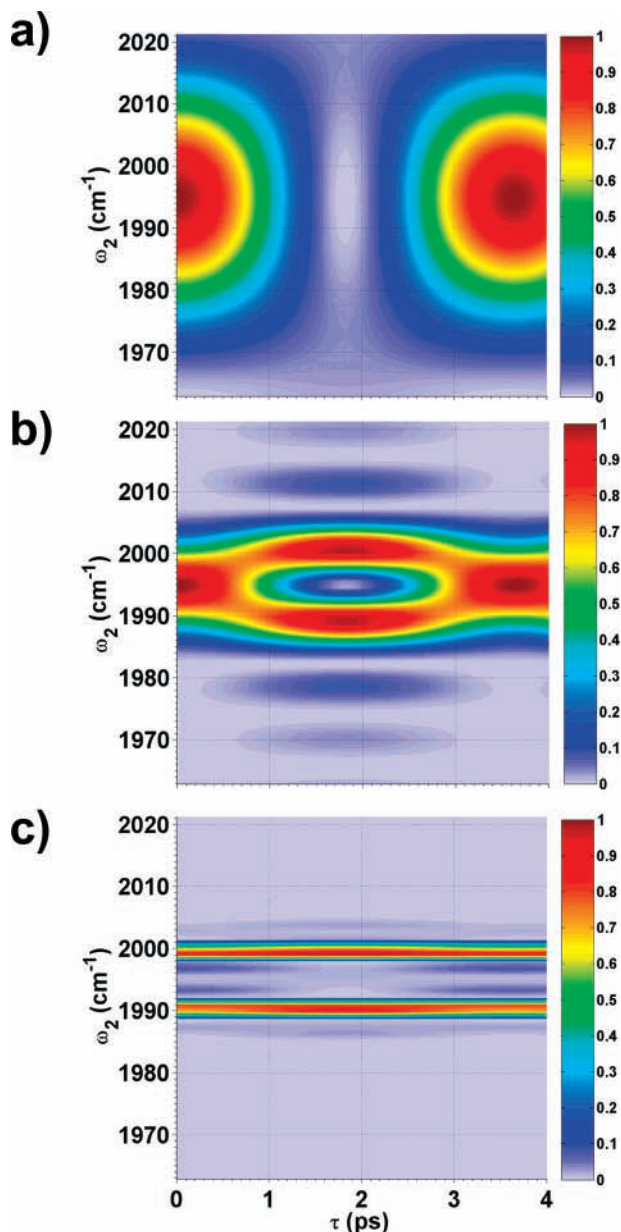


Figure 5. Two-dimensional representation of the intensity as a function of the excitation frequency and the time delay (τ) between the excitation and the measurement for a two-state system with no dephasing. The excitation is a rectangular pulse (width of 2s) where (a) $s = 0.5$ ps, (b) $s = 2$ ps, and (c) $s = 9.7$ ps. The separation between the two states corresponds to that in Table 1.

The appendix shows the corresponding equation for arbitrary times. In this simplified model, we assume that the next two interactions are impulsive and transform $\rho(\tau)$ to the output coherence, so the temporal and spectral behavior of $\rho(\tau)$ is reflected in the output. The observed intensity for homodyne detection (integration of all output signal) is then $I \propto |\rho_{\text{total}}|^2$. For clarity, we calculate the intensity when all dephasing rates are zero. Then,

$$I(\tau, \omega_2) \propto \frac{\sin^2[(\omega_{a_{1g}} - \omega_2)s]}{(\omega_{a_{1g}} - \omega_2)^2} + \frac{\sin^2[(\omega_{a_{2g}} - \omega_2)s]}{(\omega_{a_{2g}} - \omega_2)^2} + 2 \cos[(\omega_{a_{2g}} - \omega_{a_{1g}})\tau] \left\{ \frac{\sin[(\omega_{a_{1g}} - \omega_2)s] \sin[(\omega_{a_{2g}} - \omega_2)s]}{(\omega_{a_{1g}} - \omega_2)(\omega_{a_{2g}} - \omega_2)} \right\} \quad (4)$$

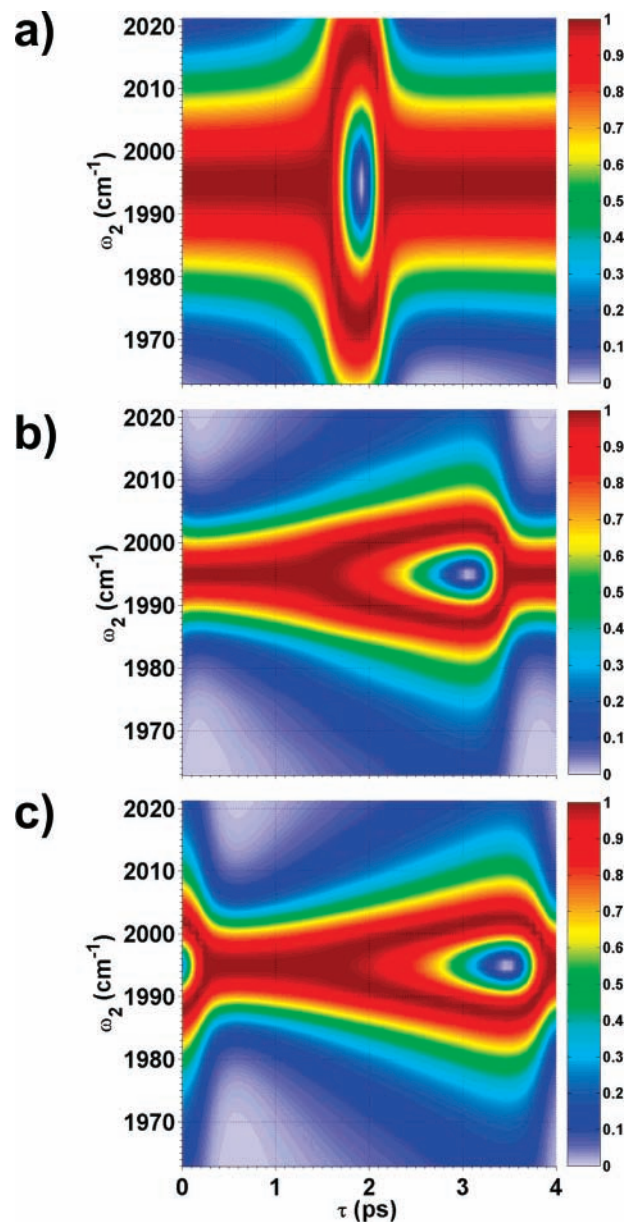


Figure 6. Two-dimensional representation of the normalized intensity as a function of the excitation frequency and the time delay (τ) between the excitation and the measurement. The intensity is normalized to the most intense feature at a given delay time. The dephasing rate corresponds to 6 cm^{-1} . Other parameters are identical to Figure 5.

The first two terms represent the individual resonances of the two vibrational states broadened by the excitation pulse bandwidth. The $\cos[(\omega_{a_{2g}} - \omega_{a_{1g}})\tau]$ in the last term is responsible for the temporal quantum beating with a period $T = 2\pi/(\omega_{a_{2g}} - \omega_{a_{1g}})$. Its amplitude is determined by the product of the two sinc functions that depend on the detuning from each resonance and the pulse width. It is this product that is responsible for the spectral quantum beating described in this paper. If $\tau = (2n + 1)\pi/(\omega_{a_{2g}} - \omega_{a_{1g}})$, $\cos[(\omega_{a_{2g}} - \omega_{a_{1g}})\tau] = -1$, and eq 4 becomes

$$I\left(\tau = \frac{(2n + 1)\pi}{(\omega_{a_{2g}} - \omega_{a_{1g}})}, \omega_2\right) \propto \left(\frac{\sin[(\omega_{a_{1g}} - \omega_2)s]}{(\omega_{a_{1g}} - \omega_2)} - \frac{\sin[(\omega_{a_{2g}} - \omega_2)s]}{(\omega_{a_{2g}} - \omega_2)} \right)^2 \quad (5)$$

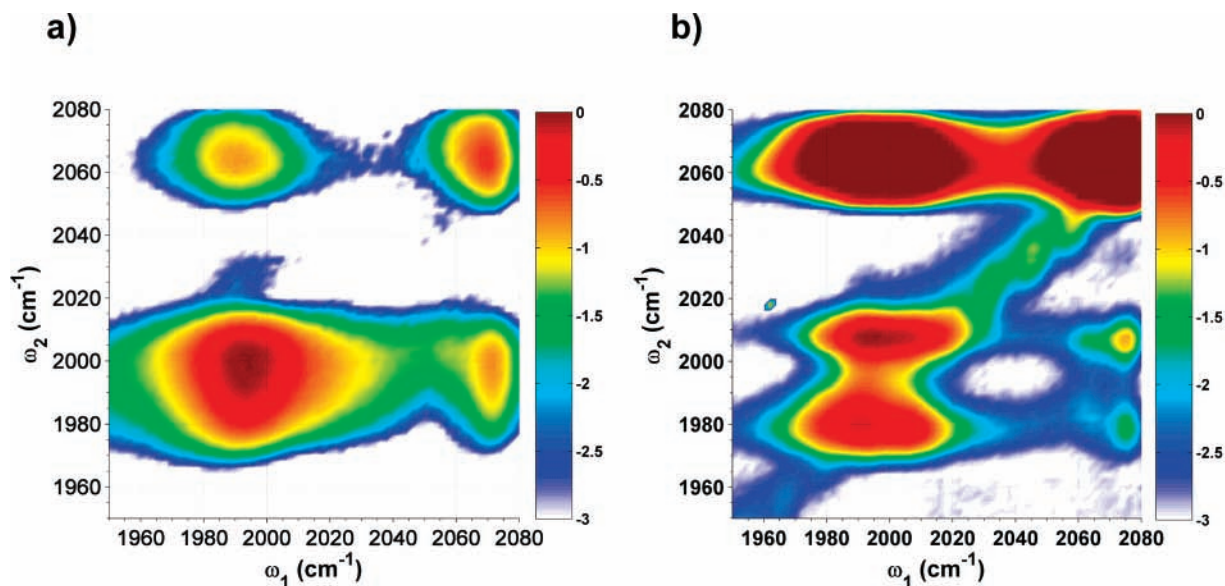


Figure 7. Two-dimensional spectra of the log(FWM intensity) as a function of ω_1 and ω_2 when $\omega_m = \omega_1$ for time ordering VI and two sets of delay times: (a) $\tau_{21} = -6.0$ ps, $\tau_{21} = -5.0$ ps and (b) $\tau_{21} = -7.6$ ps, $\tau_{21} = -5.0$ ps.

This function shows the spectral beating between the two resonances. The intensity is zero if $\omega_2 = (\omega_{a2g} - \omega_{a1g})/2$, since the two sinc functions have the same amplitude at this point. The intensity reaches a maximum at two other frequencies where one or the other state is closer to resonance, so the two sinc functions have different amplitudes. The splitting between the maxima depends on the temporal width of the excitation pulse.

Figure 5 shows how the spectral and temporal behavior of this two state system evolves as the excitation pulse width, s , varies between impulsive and cw behavior. The two-dimensional display shows the intensity as a function of the measurement time, τ , and the excitation frequency, ω_2 . Short pulses have wide bandwidths that excite both states equally, and temporal quantum beats appear. Long pulses have narrow bandwidths that excite primarily one state, so the temporal beating is weak, and the states' splitting is resolved. For intermediate pulse widths, the relative amplitude of each state depends on the excitation frequency's detuning from each state, and temporal and spectral quantum beating occurs. If $\omega_2 = (\omega_{a2g} - \omega_{a1g})/2$, both states contribute equally, and only temporal beating is observed. If $\tau = \pi/\omega_{a2g} - \omega_{a1g}$, the contribution from both states depends on the detuning from each one, and a spectral splitting occurs along the ω_2 axis. The spectral splitting appears periodically in time and has the same period.

The case when the dephasing is not zero is significantly more complex and appears in the appendix. The equation now contains factors that depend on $\cos[(\omega_{a2g} - \omega_{a1g})\tau]$ and $\sin[(\omega_{a2g} - \omega_{a1g})\tau]$, so the quantum beating occurs with the same period, but the phase is shifted by the pulse width and dephasing rates. Figure 6 shows the changes in the spectral and temporal behavior of the quantum beating for this case. In order to compensate for the signal's exponential decay, the intensity was normalized to the brightest feature at each measurement time. The spectral and temporal quantum beating become clearer with this normalization. Note the dependence of the quantum beating's phase, the changes in the maximum and minimum positions with the dephasing rate and the pulse width, and the changes in the magnitude of the splitting with the pulse width. For this case, the quantum beating is observed even for a long pulse length because the nonzero dephasing rate has broadened each transition so they spectrally overlap and interfere.

Results and Discussion

Figure 7 shows two-dimensional spectra of NTC for time ordering VI and two sets of delay times. Both spectra show the FWM intensity as a function of ω_1 and ω_2 when $\omega_m = \omega_1$. The left-hand 2D spectrum with $\tau_{21} = -6.0$ ps, $\tau_{21} = -5.0$ ps (Figure 7a) has diagonal peaks at $(\omega_1, \omega_2) \approx (2000, 2000)$ and $(2069, 2069)$ cm^{-1} corresponding to creation of *ag* and *bg* coherences, respectively, and cross-peaks at $(\omega_1, \omega_2) \approx (2000, 2069)$ corresponding to the creation of a *bg* and then an *ag* coherence and $(2069, 2000)$ cm^{-1} corresponding to creation of an *ag* and then a *bg* coherence, all of which are broadened by the presence of the other pathways. The transitions associated with the a_1 and a_2 states are not resolved; neither is there any resolution of the α and β transitions. This lack of resolution is expected since the spectral separation of the peaks is small when compared with the bandwidth of the excitation pulses.

The spectrum changes significantly, however, when τ_{21} is increased to -7.6 ps (Figure 7b). This change corresponds to an increase in the delay time between the first and second pulses from 1.0 to 2.6 ps. There are two consequences. First, the upper set of peaks is much stronger than the lower set of peaks. This difference is caused because the *bg* coherence that results from the first pulse in the upper set of peaks has a slower dephasing rate than the *ag* coherence formed for the lower set of peaks. Consequently, the *bg* coherence does not decay as quickly, so the peaks that result from the *bg* coherence are stronger. Second, the lower set of peaks at $(\omega_1, \omega_2) \approx (2000, 2000)$ and $(2069, 2000)$ cm^{-1} split into two different sets of peaks in the ω_2 dimension. The lower row of peaks is located at $\omega_2 \approx 1980$ cm^{-1} , and the upper row, at $\omega_2 \approx 2007$ cm^{-1} . These positions do not correspond to any peaks in the FTIR data and indicate the presence of frequency-domain quantum beating between *a1g* and *a2g* coherences formed by the first excitation pulse. There is no splitting or quantum beating for the upper set of peaks since the first coherence is a single *bg* coherence.

Figure 8 is a two-dimensional display of the FWM intensity as a function of τ_{21} and ω_2 with fixed values of $\tau_{21} = -5.0$ ps and $\omega_1 = \omega_m = 2069$ cm^{-1} . It shows both the spectral and temporal beating. Figure 8a shows the logarithm of the FWM intensity; Figure 8b renormalizes the logarithm of the FWM intensity to the maximum value at $\tau_{21} = -7.0$ ps; Figure 8c

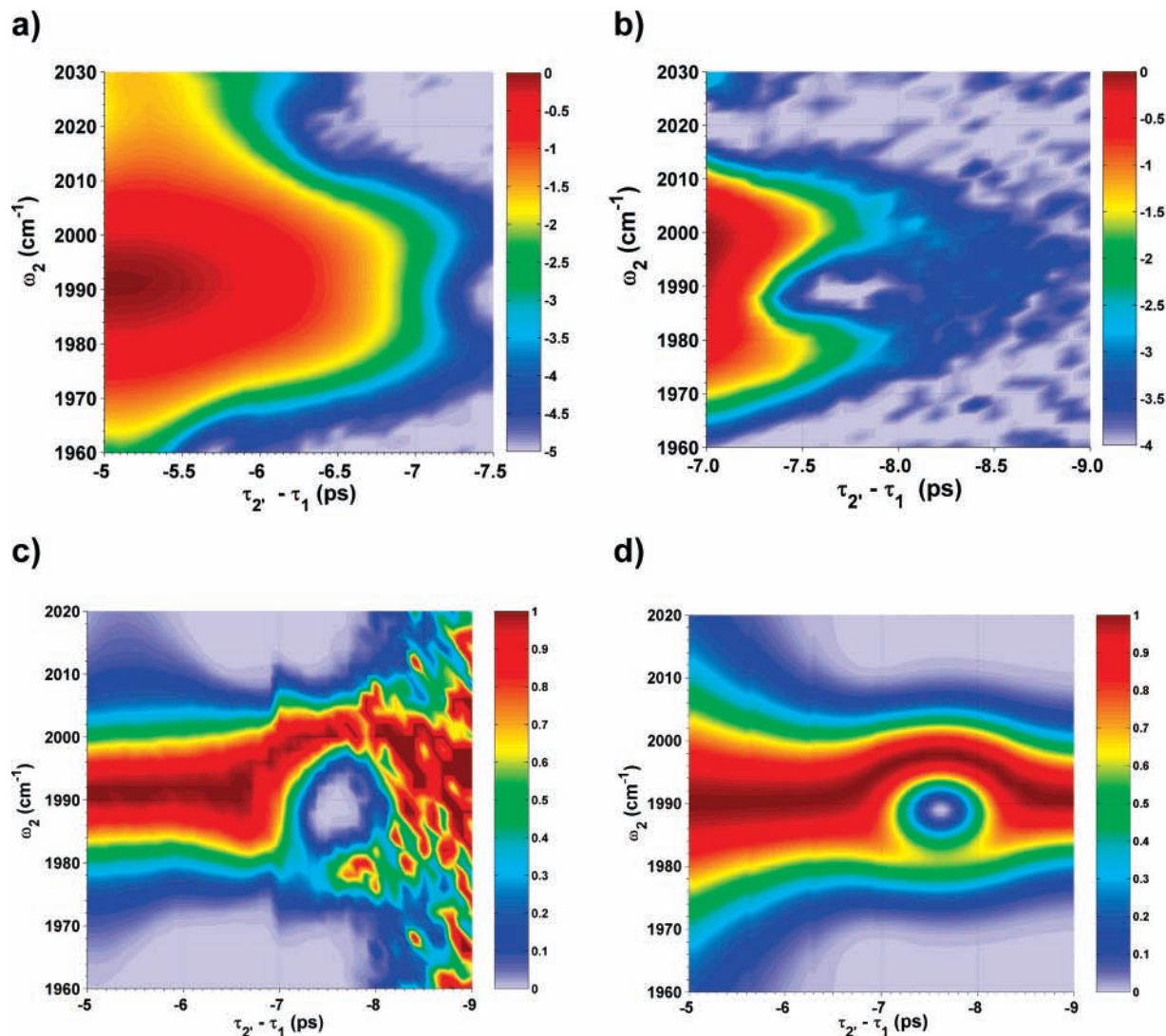


Figure 8. Two-dimensional representation of the log(FWM intensity) as a function of τ_{21} and ω_2 with a fixed value of $\omega_1 = 2069 \text{ cm}^{-1}$. Parts a, b, and c are taken under identical conditions. The data in b was obtained by resetting the signal amplification to maximize the FWM intensity at $\tau_{21} = -7.0 \text{ ps}$ and enhance the signal at long delay times. The color bar again represents the log(FWM intensity). The FWM intensity has been renormalized in c to the peak intensity at any given τ_{21} to observe how the spectral shapes and positions change with delay time. The color bar represents the FWM intensity. Part d is a simulation of the renormalized data using the method described in the text and the parameters in Table 1. It should be compared to part c.

renormalizes the data in a and b to the maximum of the FWM intensity for each τ_{21} value. At $\tau_{21} = -5.0 \text{ ps}$, there is a single broad peak at $\omega_2 = 2000 \text{ cm}^{-1}$. The peak splits into two peaks at $\tau_{21} = -7.8 \text{ ps}$ that then recombine at $\tau_{21} = -8.4 \text{ ps}$. These observations indicate the interference is not constant, but periodic. The splitting is not symmetric. The higher energy peak is stronger than the lower energy peak. A similar pattern of splitting and recombination occurs with the $\alpha 1$, $\alpha 2$, $\alpha 8$, and $\alpha 9$ pathways (data not shown).

The quantum beating occurs in TRIVE because the two different coherences excited by the first pulse have different phases when the second pulse interacts and can constructively or destructively interfere. Quantum beating is not seen between the coherences that result after the third pulse because the experiment does not temporally resolve the output coherence. Consequently, beating is not observed along the ω_1 axis, even when the a_{1g} and a_{2g} coherences are excited. Figure 8d shows a simulation of the temporal and spectral quantum beating using a numerical integration of eq 1 assuming Gaussian shaped pulses. Note that the splitting in the simulations is not symmetric. The asymmetry is due to differences in the dephasing rates for

TABLE 1: Parameter Values Used to Simulate Experimental Data

$\omega_{a_{2,g}} - \omega_{a_{1,g}}$	9 cm^{-1}
σ^a	7.6 cm^{-1}
$\Gamma_{a_{1,g}}$	6.5 cm^{-1}
$\Gamma_{a_{2,g}}$	6.15 cm^{-1}
$\Gamma_{b,g}$	2.25 cm^{-1}
$\Gamma_{g,g}$	0.2 cm^{-1}

^a Standard deviation of Gaussian excitation pulse.

the two coherences. The higher energy peak has a slightly slower dephasing rate, and consequently, its intensity is higher. The frequency difference and the dephasing rates for the simulation are summarized in Table 1. Their values match those obtained by fitting the line shapes of the FTIR spectra. The frequency difference of 9 cm^{-1} would correspond to a quantum beating period of 3.7 ps. If the excitation pulse were impulsive, the intensity minimum would occur at a 1.85 ps delay (corresponding to $\tau_{21} = -6.85 \text{ ps}$). Instead, Figure 8 shows it appears at 2.75 ps ($\tau_{21} = -7.75 \text{ ps}$). This shift is matched by the simulation that shows that the difference is caused by the phase shift in

the quantum beating from the finite widths of the excitation pulses and dephasing rates.

Conclusions

Mixed frequency/time-domain coherent multidimensional spectra exhibit a time- dependent spectral splitting between unresolved quantum states that result from quantum beating between quantum states that are simultaneously excited, either because they overlap spectrally or because the excitation pulse bandwidth is broader than their frequency difference. The quantum beating creates a line shape that depends on the delay time between excitation pulses and a splitting that depends on the excitation pulse bandwidth. The spectral quantum beating allows the mixed frequency/time-domain methods such as DOVE and TRIVE-FWM to resolve quantum states that are not resolved in conventional one-dimensional spectra.

Acknowledgment. This work was supported by the National Science Foundation under Grant CHE-0650431. Acknowledgment is also made to the donors of the Petroleum Research Fund of the American Chemical Society for their support of this research. This work was supported in part by a fellowship from Merck Research Laboratories. A.V.P. and M.A.R. contributed equally to this reported research.

Appendix

Equation 3 was derived from eq 2 under the assumption that $\tau > s$. The more general equation is

$$\rho(\tau) = \frac{e^{-i\omega_{a,b}\tau - \Gamma_{a,b}\tau}}{i\Delta_{a,b} + \Gamma_{a,b}} [(e^{-i\omega_{a,b}\tau - \Gamma_{a,b}\tau} - e^{-i\Delta_{a,b}s - \Gamma_{a,b}s}) \theta(s - \tau) + (e^{i\Delta_{a,b}s + \Gamma_{a,b}s} - e^{-i\Delta_{a,b}s - \Gamma_{a,b}s}) \theta(\tau - s)] \theta(\tau + s) \quad (3')$$

Equation 4 was derived from eq 3 if the dephasing rates were zero. The more general equation is

$$I(\tau, \omega_2) \propto F_1 + F_2[F_3(F_{4a} + F_{4b}) + F_5(F_{6a} + F_{6b})] \quad (4')$$

where

$$F_1 = \frac{e^{-2\Gamma_{a1}\tau}}{\Delta_{a1}^2 + \Gamma_{a1}^2} [\cosh(2\Gamma_{a1}s) - \cos(2\Delta_{a1}s)] + \frac{e^{-2\Gamma_{a2}\tau}}{\Delta_{a2}^2 + \Gamma_{a2}^2} [\cosh(2\Gamma_{a2}s) - \cos(2\Delta_{a2}s)]$$

$$F_2 = \frac{4e^{-(\Gamma_{a1} + \Gamma_{a2})\tau}}{(\Delta_{a1}^2 + \Gamma_{a1}^2)(\Delta_{a2}^2 + \Gamma_{a2}^2)}$$

$$F_3 = \cos(\Delta_{a1}s) \sinh(\Gamma_{a1}s)$$

$$F_{4a} = \sin(\Delta_{a2}s) \cosh(\Gamma_{a2}s) [- (\Delta_{a1}\Delta_{a2} + \Gamma_{a1}\Gamma_{a2}) \sin(\omega_{a1,a2}\tau) + (\Delta_{a2}\Gamma_{a1} - \Delta_{a1}\Gamma_{a2}) \cos(\omega_{a1,a2}\tau)]$$

$$F_{4b} = \cos(\Delta_{a2}s) \sinh(\Gamma_{a2}s) [(\Delta_{a1}\Delta_{a2} + \Gamma_{a1}\Gamma_{a2}) \cos(\omega_{a1,a2}\tau) + (\Delta_{a2}\Gamma_{a1} - \Delta_{a1}\Gamma_{a2}) \sin(\omega_{a1,a2}\tau)]$$

$$F_5 = \sin(\Delta_{a1}s) \cosh(\Gamma_{a1}s)$$

$$F_{6a} = \sin(\Delta_{a2}s) \cosh(\Gamma_{a2}s) [(\Delta_{a1}\Delta_{a2} + \Gamma_{a1}\Gamma_{a2}) \cos(\omega_{a1,a2}\tau) + (\Delta_{a2}\Gamma_{a1} - \Delta_{a1}\Gamma_{a2}) \sin(\omega_{a1,a2}\tau)]$$

$$F_{6b} = \cos(\Delta_{a2}s) \sinh(\Gamma_{a2}s) [(\Delta_{a1}\Delta_{a2} + \Gamma_{a1}\Gamma_{a2}) \sin(\omega_{a1,a2}\tau) + (\Delta_{a1}\Gamma_{a2} - \Delta_{a2}\Gamma_{a1}) \cos(\omega_{a1,a2}\tau)]$$

References and Notes

- (1) Hack, E.; Huber, J. R. *Int. Rev. Phys. Chem.* **1991**, *10*, 287.
- (2) Haroche, S.; Paisner, J. A.; Schawlow, A. L. *Phys. Rev. Lett.* **1973**, *30*, 948.
- (3) Bitto, H.; Huber, J. R. *Acc. Chem. Res.* **1992**, *25*, 65.
- (4) Carter, R. T.; Huber, J. R. *Chem. Soc. Rev.* **2000**, *29*, 305.
- (5) Wright, J. C.; Condon, N. J.; Murdoch, K. M.; Besemann, D. M.; Meyer, K. A. *J. Phys. Chem. A* **2003**, *107*, 8166.
- (6) Jonas, D. M. *Annu. Rev. Phys. Chem.* **2003**, *54*, 425.
- (7) Mukamel, S. *Annu. Rev. Phys. Chem.* **2000**, *51*, 691.
- (8) Cho, M. Two Dimensional Vibrational Spectroscopy. In *Advances in Multi-Photon Processes and Spectroscopy*, 1st ed.; Lin, S. H.; Villaeys, A. A.; Fujimura, Y., Eds.; World Scientific: Singapore 1999; Vol. 12, pp 1.
- (9) Condon, N. J.; Wright, J. C. *J. Phys. Chem. A* **2005**, *109*, 721.
- (10) Murdoch, K. M.; Condon, N. J.; Zhao, W.; Besemann, D. M.; Meyer, K. A.; Wright, J. C. *Chem. Phys. Lett.* **2001**, *335*, 349.
- (11) Zhao, W.; Wright, J. C. *Phys. Rev. Lett.* **2000**, *84*, 1411.
- (12) Zhao, W.; Wright, J. C. *J. Am. Chem. Soc.* **1999**, *121*, 10994.
- (13) Zhao, W.; Wright, J. C. *Phys. Rev. Lett.* **1999**, *83*, 1950.
- (14) Rickard, M. A.; Pakoulev, A. V.; Kornau, K.; Mathew, N. A.; Wright, J. C. *J. Phys. Chem. A* **2006**, *110*, 11384.
- (15) Pakoulev, A. V.; Rickard, M. A.; Meyers, K. A.; Kornu, K.; Mathew, N. A.; Thompson, D. C.; Wright, J. C. *J. Phys. Chem. A* **2006**, *110*, 3352.
- (16) Meyer, K. A.; Thompson, D. E.; Wright, J. C. *J. Phys. Chem. A* **2004**, *108*, 11485.
- (17) Meyer, K. A. Frequency-Scanned Ultrafast Spectroscopic Techniques Applied to Infrared Four-Wave Mixing Spectroscopy; Ph. D. Dissertation. University of Wisconsin-Madison, 2004.
- (18) Besemann, D. M.; Meyer, K. A.; Wright, J. C. *J. Phys. Chem. B* **2004**, *108*, 10493.
- (19) Meyer, K. A.; Wright, J. C. *Chem. Phys. Lett.* **2003**, *381*, 642.
- (20) Mukamel, S. *Principles of Nonlinear Optical Spectroscopy*, 1st ed.; Oxford University Press: New York, 1995.